

# CRISM LIMB OBSERVATIONS OF MARS O<sub>2</sub>/OH POLAR NIGHTGLOW AND O<sub>2</sub> DAYGLOW, AND THEIR COMPARISON TO LMD GCM PHOTOCHEMICAL SIMULATIONS

**R. T. Clancy, B. J. Sandor, M. J. Wolff, SSI, Boulder, CO, USA** ([clancy@spacescience.org](mailto:clancy@spacescience.org)), **F. Lefèvre, LATMOS, Paris, France**, **A. García-Muñoz, ESA/RSSD, ESTEC, Netherlands**, **M. D. Smith, T. H. McConnochie, GSFC, Greenbelt, MD, USA**, **S. L. Murchie and Hari Nair, JHU/APL, Columbia, MD, USA**.

## Introduction:

Targeted CRISM<sup>1</sup> (Compact Reconnaissance Imaging Spectrometer for Mars) limb observations from the Mars Reconnaissance Orbiter (MRO) began in July 2009, and have since obtained extensive vertical profiling of Mars atmospheric constituents [dust and ice opacities<sup>2</sup>, O<sub>2</sub>(<sup>1</sup>Δ<sub>g</sub>)<sup>3,4</sup>, OH<sup>5</sup>] versus season (solar longitude-L<sub>s</sub>), latitude, and longitude. CRISM limb observations return visible and near-infrared ( $\lambda \sim 0.4\text{--}4 \mu\text{m}$ ) spectra with modest spectral resolution ( $\Delta\lambda \sim 0.01 \mu\text{m}$ ) and high vertical resolution (0.5 km)<sup>3</sup>.

Although designed to measure surface and atmospheric spectra in full solar illumination, CRISM near-IR limb spectra detect nightglow by O<sub>2</sub> and OH over polar night conditions at 40–65 km altitudes (figure 1). These extensive polar night observations of O<sub>2</sub>(<sup>1</sup>Δ<sub>g</sub>) provide a detailed seasonal and spatial characterization of the 1.27 μm (0-0) band emission as well as the first detection of the 1.58 μm (0-1) band emission<sup>3,4</sup>. CRISM polar night observations of OH Meinel band<sup>6</sup> emission (figure 1) constitute the first detection of the key OH photochemical radical in the Mars atmosphere<sup>5</sup>.

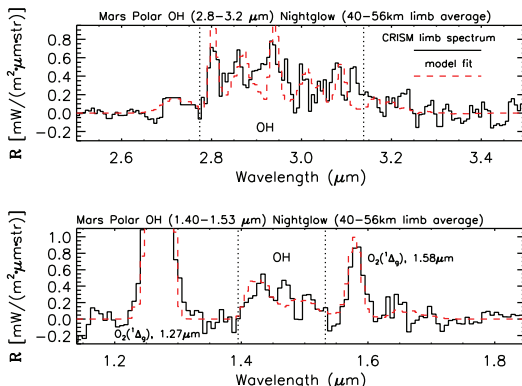


Figure 1. Best-fit (red-dashed) and CRISM average winter polar limb spectra (black-solid) for O<sub>2</sub> and OH nightglow exhibit near-IR O<sub>2</sub>(<sup>1</sup>Δ<sub>g</sub>) (strong at 1.27 μm, R<sub>peak</sub>=55; weak at 1.58 μm) and OH (weak over 1.4–1.7 μm and 2.8–3.2 μm) band emissions<sup>5</sup>.

Both the OH and O<sub>2</sub>(<sup>1</sup>Δ<sub>g</sub>) polar night emissions result from upper level (>50 km) meridional transport of dayside O and H photo-dissociation products into the polar fall-winter-spring atmosphere, where they descend to recombine as O<sub>2</sub> and OH electronically/vibrationally excited species. These CRISM polar nightglow observations have been compared to LMD (Laboratoire de

Météorologie Dynamique) GCM (Global Climate Model) simulations incorporating detailed photochemistry<sup>7,8</sup>, to provide new constraints on Mars atmospheric transport, chemistry, and molecular physics<sup>3,4,5</sup>.

More recently, CRISM limb profiles of O<sub>2</sub>(<sup>1</sup>Δ<sub>g</sub>) 1.27 μm dayglow have been retrieved to provide the first extensive (versus L<sub>s</sub>, full latitude and 1–3 longitudes) definition of the vertical dependence of O<sub>2</sub>(<sup>1</sup>Δ<sub>g</sub>) volume emission rates (VER). These dayside O<sub>2</sub> VER profiles reflect the O<sub>3</sub> vertical distribution in that O<sub>2</sub>(<sup>1</sup>Δ<sub>g</sub>) dayglow results from O<sub>3</sub> photodissociation<sup>9</sup>. The observed vertical extent of O<sub>2</sub> VER below 20 km altitudes also constrains the uncertain collisional de-excitation rate coefficient for O<sub>2</sub>(<sup>1</sup>Δ<sub>g</sub>) in a CO<sub>2</sub> atmosphere<sup>10</sup>.

## Polar O<sub>2</sub>(<sup>1</sup>Δ<sub>g</sub>) Nightglow:

As depicted in figure 2, O<sub>2</sub>(<sup>1</sup>Δ<sub>g</sub>) emission originates in the Mars atmosphere from two distinct formation mechanisms:

- (1) O<sub>3</sub> + hν → O<sub>2</sub>(<sup>1</sup>Δ<sub>g</sub>) + O
- (2) O + O + CO<sub>2</sub> → O<sub>2</sub>(<sup>1</sup>Δ<sub>g</sub>) + CO<sub>2</sub>

Branching ratios for O<sub>2</sub>(<sup>1</sup>Δ<sub>g</sub>) production from reactions 1–2 and radiative factors for O<sub>2</sub>(<sup>1</sup>Δ<sub>g</sub>) band emission are known well enough to calculate accurate ( $\pm 10\%$ ) 1.27 μm emission rates from LMD GCM simulated photochemical fields<sup>3</sup>.

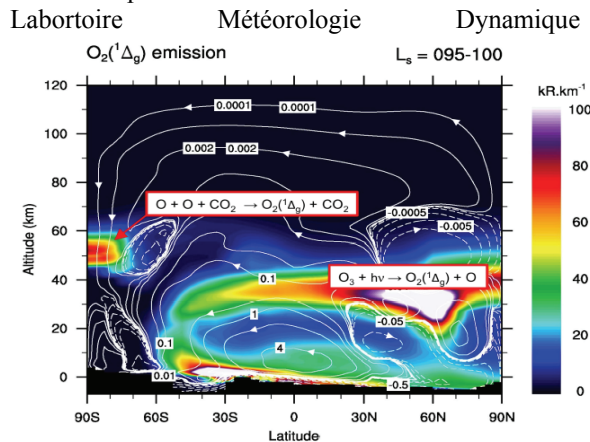


Figure 2. Latitude/altitude schematic of LMD GCM simulated transport and O<sub>2</sub>(<sup>1</sup>Δ<sub>g</sub>) VER for southern winter, for dayglow (reaction 1) and polar nightglow (reaction 2)<sup>3</sup>.

Although reaction (1) has long been associated with ground-based and spacecraft observations of

Mars 1.27 $\mu\text{m}$  dayglow, the role of reaction (2) in Mars polar 1.27 $\mu\text{m}$  nightglow has only recently been recognized. CRISM<sup>3,4</sup>, OMEGA<sup>11</sup>, and SPICAM<sup>12</sup> limb observations detected polar night 1.27  $\mu\text{m}$  emission at 40-65km altitudes, quickly associated with meridional transport of O to the winter poles and  $\text{O}_2(^1\Delta_g)$  production via reaction 2. Figure 2 depicts Mars atmospheric circulation and photochemistry at  $L_s=95\text{-}100^\circ$ , leading to Mars southern (winter) polar  $\text{O}_2(^1\Delta_g)$  nightglow at 40-60km, and southern mid-latitude to northern (summer) polar  $\text{O}_2(^1\Delta_g)$  dayglow. Polar  $\text{O}_2(^1\Delta_g)$  nightglow is also present near the poles in equinoctial seasons.

Profile retrieval analyses of polar nightglow limb measurements are relatively straight-forward as atmospheric scattering/absorption effects are negligible and, hence, multiple scattering radiative transfer (RT) is unnecessary<sup>3,12</sup>. Figure 3 presents a set of individual CRISM profile retrievals for 1.27 $\mu\text{m}$  polar nightglow, indicating the seasonal variation and vertical dependence of the  $\text{O}_2(^1\Delta_g)$  polar nightglow. The

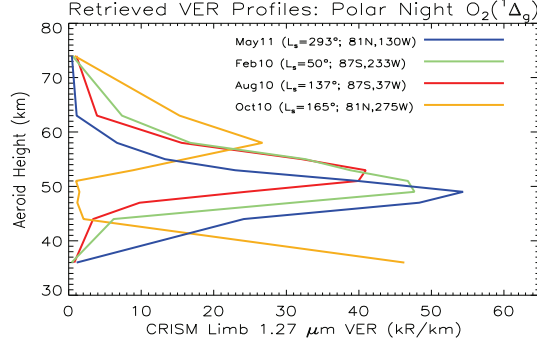


Figure 3. CRISM  $\text{O}_2(^1\Delta_g)$  polar nightglow profiles, retrieved for four distinct Mars seasons ( $1\sigma = 4\text{kR}/\text{km}$ )<sup>4</sup>.

twilight  $L_s=165^\circ$  profile includes a lower altitude dayglow contribution. All CRISM 1.27 $\mu\text{m}$  VER values have been corrected for an earlier scaling error<sup>4</sup>.

Polar 1.27 $\mu\text{m}$  nightglow limb observations by CRISM, OMEGA, and SPICAM agree within their distinct coverages and resolutions. CRISM limb polar  $\text{O}_2(^1\Delta_g)$  nightglow observations (>100) extend over a fairly complete range of latitudes and seasons

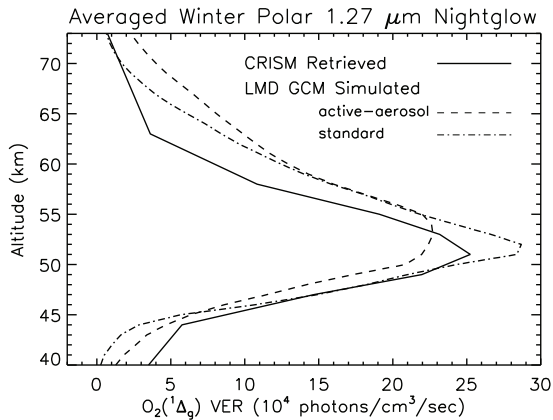


Figure 4. The CRISM observed average winter polar  $\text{O}_2(^1\Delta_g)$  profile (solid) is compared to equivalent winter averages from the LMD GCM standard (dash-dotted) and interactive (dashed) models<sup>5</sup>.

in comparison to the relatively few (~10) OMEGA and SPICAM limb observations, and so have supported a detailed comparison with LMD GCM simulations of polar  $\text{O}_2(^1\Delta_g)$  nightglow<sup>3,4</sup>. The transport sensitivity of the polar  $\text{O}_2(^1\Delta_g)$  nightglow was investigated by employing GCM simulations without (standard) and with (interactive) radiatively active clouds and interactive dust profiles<sup>13,14</sup>. Model and observed  $\text{O}_2(^1\Delta_g)$  profiles are quite similar in average polar winter solstice behavior, as are model results for standard and interactive simulations (figure 4). However, periods away from winter solstice (e.g.,  $L_s=137^\circ$ ,  $166^\circ$ , and  $193^\circ$ ) are significantly better fit by the interactive LMD GCM simulation<sup>3,4</sup>, as demonstrated in figures 5 and 6.

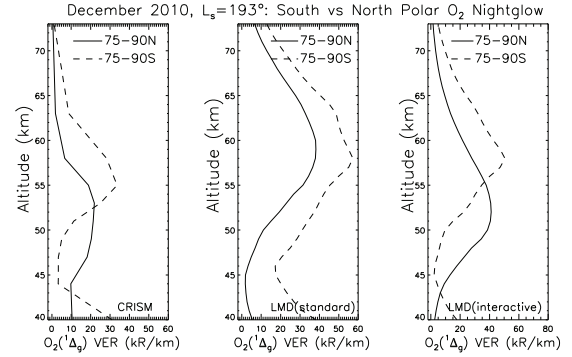


Figure 5. Equinox averaged CRISM (left)  $\text{O}_2(^1\Delta_g)$  VER profiles are compared to LMD GCM simulations without (center) and with (right) interactive aerosol forcing<sup>3,4</sup>.

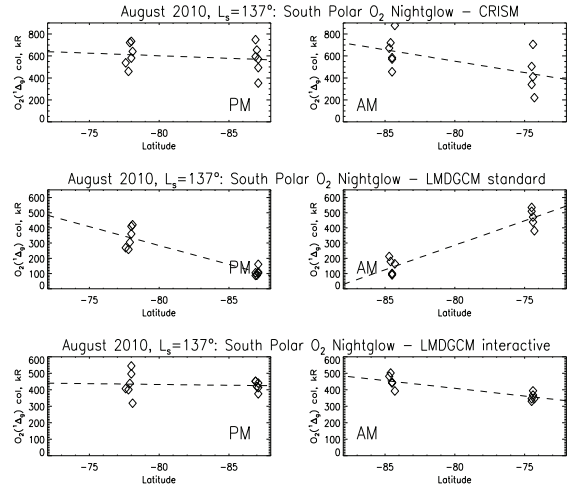


Figure 6. Late winter ( $L_s=137^\circ$ ) SP latitudinal variations in vertically integrated  $\text{O}_2(^1\Delta_g)$  VER from retrieved CRISM profiles (top), compared to LMD GCM simulations without (center) and with (bottom) interactive aerosol forcing<sup>4</sup>.

At equinox, CRISM  $\text{O}_2(^1\Delta_g)$  VER vertical profiles (figure 5, left) are much better simulated by the interactive simulation (figure 5, right). In late southern winter ( $L_s=137^\circ$ ), the latitudinal dependence of the  $\text{O}_2(^1\Delta_g)$  column nightglow (figure 6, top) is also

much better fit by the interactive model (figure 6, bottom). The interactive LMD GCM simulated winter polar temperature profiles are also more consistent with MCS retrieved profiles<sup>15</sup> at this time<sup>3</sup>. Nevertheless, the CRISM winter solstice average profile of  $O_2(^1\Delta_g)$  is well produced by either LMD GCM model (figure 4), demonstrating remarkable consistency with the coupled winter hemisphere upper level transport and  $O_x$  ( $O + O_3$ ) photochemistry incorporated in the LMD GCM simulations<sup>4,5</sup>. The detailed seasonal and spatial/temporal variations of  $O_2(^1\Delta_g)$  polar nightglow are driven primarily by variable poleward-descent transport of upper level O, which is affected by the large-scale distribution of dust and cloud radiative forcing<sup>3</sup>. In addition, the observed temperature dependence of the polar night VER derived from co-located MCS temperature profiles compares well to model simulations employing the Roble<sup>16</sup> collisional rate constant expression for reaction (2)<sup>3</sup>.

#### Polar OH Nightglow:

A grand average of CRISM polar winter limb spectra (figure 1) provides the first Mars measurement of the key OH radical<sup>5</sup>, a primary agent of the  $HO_x$  catalytic cycle that recombines CO and  $O_2$  products of bulk atmosphere ( $CO_2$ ) photolysis<sup>17,18</sup> and regulates loss of associated  $O_x$  products<sup>19,20</sup>. Polar OH nightglow results from combined H and O poleward transport within the same meridional upper level circulation responsible for driving  $O_2(^1\Delta_g)$  polar nightglow (figure 1). In this case, three reactions

- (3)  $O + O_2 + CO_2 \rightarrow O_3 + CO_2$
- (4)  $O_3 + H \rightarrow O_2 + OH^*$
- (5)  $O + HO_2 \rightarrow O_2 + OH^*$

are most relevant to the production of OH in vibrationally excited Meinel bands. A distinctive winter polar peak in  $O_3$  at 40-60km, recently observed by SPICAM, is attributed to reaction (3) and the same upper level poleward transport of O resulting in polar  $O_2(^1\Delta_g)$  nightglow<sup>21</sup>. Reaction (4), the Bates-Nicolet mechanism<sup>22</sup>, is inferred to predominate over reaction (5) in terrestrial OH emission due to larger mesospheric H (vs  $HO_2$ ) densities as well as the observed OH band emission distribution<sup>23</sup>.

As indicated in figures 7 and 8, Mars OH Meinel emissions detected in CRISM averaged winter polar limb spectra (figure 1) only provide  $2\sigma$  detections for the (1-0), (2-1), and (2-0) bands, with  $1\sigma$  detection or upper limits for 4 additional bands<sup>5</sup>. The observed Mars OH band ratios, intensities, and vertical profile dependences (figure 8) suggest that the Bates-Nicolet mechanism is the most important source of Mars Meinel band OH emission<sup>5</sup>. Another important process in modeling OH band emission is that of collisional quenching on vibrational energy transfer, for which two distinct pathways have been consid-

ered for Mars<sup>24</sup>. The CRISM OH limb spectrum determines that ‘collisional-cascade’ (CC) rather than ‘sudden-death’ vibrational quenching operates in the Mars polar night<sup>5</sup>.

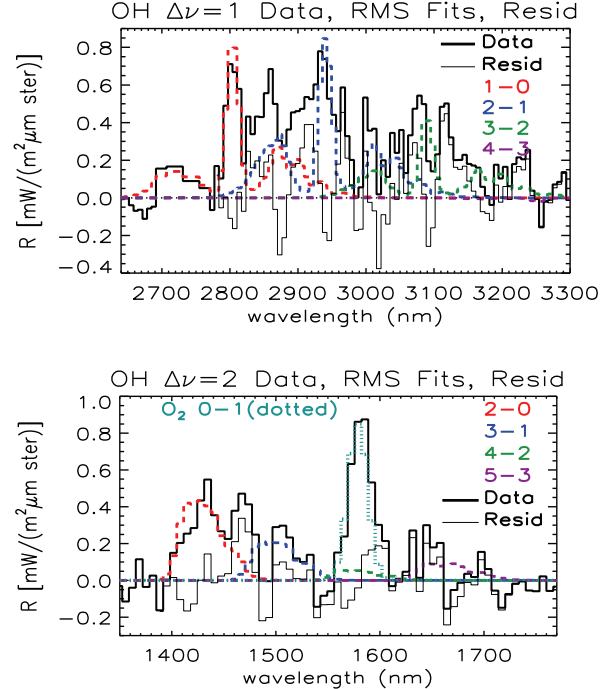


Figure 7. The CRISM observed and Meinel band fit model for near-IR OH limb emission in Mars polar winter at 40-56km altitudes. The band-summed model fit is provided by the red line in figure 2. The (1-0), (2-1), and (2-0) OH Meinel bands, as well as the (0-1) band of  $O_2(^1\Delta_g)$ , are adequately determined by the CRISM measurement<sup>5</sup>.

Both the averaged CRISM polar winter OH (figure 8) and  $O_2(^1\Delta_g)$  (figure 4) measurements are reasonably well fit by LMD GCM simulated photochemistry and transport. This provides significant support for modeled upper level (above 40 km)  $HO_x$  and  $O_x$  abundances and meridional circulation over the Mars winter hemisphere. Upper level  $HO_x$  and  $O_x$  consistency reflects on model upper level water vapor concentrations as well as the detailed photochemical reaction set. We also note that the best-fit  $O_2(^1\Delta_g)$  band emission ratio,  $A_{00}/A_{01} \sim 50$ , from the CRISM limb averaged spectrum (figures 1 and 7) is consistent within error bars to that measured for the Venus upper atmosphere<sup>25</sup>.

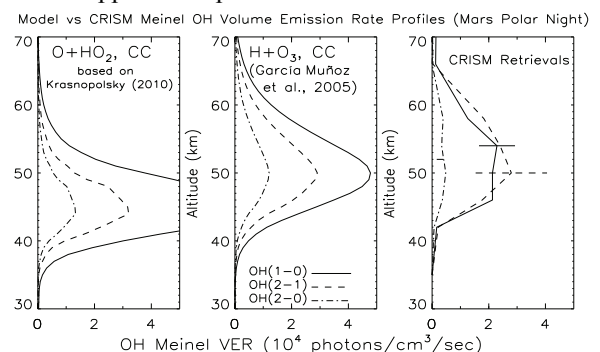


Figure 8. The CRISM retrieved profiles of OH emission in three Meinel bands (right) are compared to GCM LMD

simulations employing collisional-cascade (CC) quenching with (left) an upper limit estimate for OH\* production by reaction (5)<sup>26</sup> versus nominal production (center) via the Bates-Nicolet mechanism of reaction (4)<sup>5</sup>.

### Ozone-Related O<sub>2</sub>(<sup>1</sup>Δ<sub>g</sub>) Dayglow:

Most recently, we have retrieved vertical profiles of O<sub>2</sub>(<sup>1</sup>Δ<sub>g</sub>) VER in dayglow from extensive (2009–2013) CRISM profile observations of the illuminated atmospheric limb. Such O<sub>2</sub>(<sup>1</sup>Δ<sub>g</sub>) emission results fairly directly from O<sub>3</sub> photolysis [reaction (1)], and so places strong constraints on dayside O<sub>x</sub>. Profile retrievals from Mars O<sub>2</sub>(<sup>1</sup>Δ<sub>g</sub>) dayglow limb measurements require multiple scattering RT calculations, associated with scattering/extinction by often vertically extended aerosols (cloud and dust) as well as enhanced CO<sub>2</sub> absorption at altitudes below 40 km. We (T. McConnochie) have adapted the discrete ordinates limb RT code, employed for CRISM limb aerosol (dust and ice) retrievals<sup>2</sup>, to incorporate O<sub>2</sub>(<sup>1</sup>Δ<sub>g</sub>) volume emission. Chi-squared minimization (Levenberg-Marquardt) solutions for the O<sub>2</sub>(<sup>1</sup>Δ<sub>g</sub>) VER profile are obtained with this modified RT code, employing aerosol distributions retrieved self-consistently from the same CRISM limb spectra<sup>2</sup>.

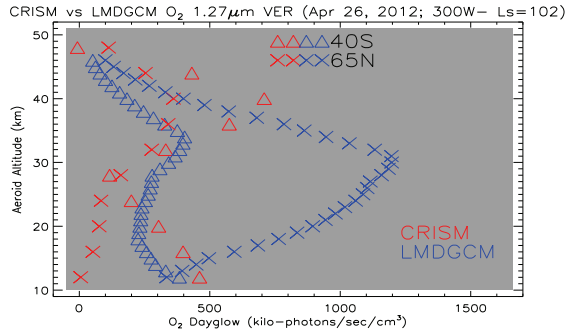


Figure 9. Vertical profiles of O<sub>2</sub>(<sup>1</sup>Δ<sub>g</sub>) dayglow VER for 40S ( $\Delta$ ) and 65N ( $\times$ ) latitudes (300W,  $L_s=102^\circ$ ) are compared from CRISM retrievals (red) and LMD GCM simulations (blue). Similar comparisons result at 70W and 0W longitudes.

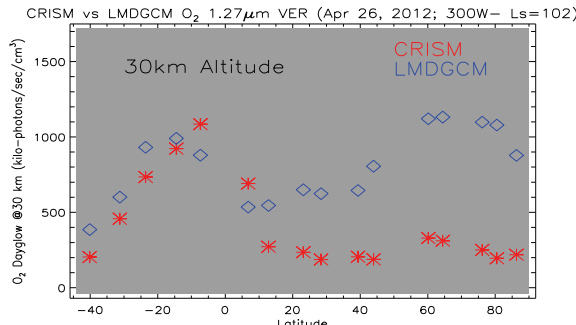


Figure 10. The latitudinal dependence of CRISM observed (red) and LMD GCM modeled (blue) O<sub>2</sub>(<sup>1</sup>Δ<sub>g</sub>) dayglow VER at 30 km altitude, 300W longitude, and  $L_s=102^\circ$ .

Preliminary comparisons of CRISM O<sub>2</sub>(<sup>1</sup>Δ<sub>g</sub>) dayglow profile retrievals to LMD GCM simulated O<sub>2</sub>(<sup>1</sup>Δ<sub>g</sub>) dayglow indicate distinct areas of agreement and disagreement, as indicated by figures 9 and 10. Aphelion northern latitude O<sub>2</sub>(<sup>1</sup>Δ<sub>g</sub>) dayglow and O<sub>3</sub>

columns<sup>27</sup> are generally observed to be lower than currently modeled, indicating insufficient water vapor in LMD GCM simulations of the northern summer atmosphere. The larger set of such O<sub>2</sub>(<sup>1</sup>Δ<sub>g</sub>) vertical profile comparisons (600 CRISM profiles, of which 30–40% yield O<sub>2</sub>(<sup>1</sup>Δ<sub>g</sub>) VER detections) should illuminate additional seasonal and latitudinal dependences for model/data disagreements in O<sub>3</sub> column abundance, as well as provide new constraints on O<sub>2</sub>(<sup>1</sup>Δ<sub>g</sub>) collisional de-excitation rates at altitudes below 20 km.

### Bibliography:

- (1) Murchie et al., JGR, v112, 2007.
- (2) Smith et al., JGR, v118, 2013.
- (3) Clancy et al., JGR, v117, 2012.
- (4) Clancy et al., JGR, v118, 2013.
- (5) Clancy et al., Icarus, v226, 2013.
- (6) Meinel, ApJ, v111 and 112, 1950.
- (7) Lefèvre et al., JGR, 109, 2004.
- (8) Lefèvre et al., Nature, 454, 2008.
- (9) Noxon et al., ApJ, v207, 1976.
- (10) Krasnopolsky&Bjoraker, JGR, v105, 2000.
- (11) Fedoraova et al., Icarus, v219, 2012.
- (12) Bertaux et al., JGR, v117, 2012.
- (13) Madeleine et al., GRL, v39, 2012.
- (14) Madeleine et al., JGR, v116, 2011
- (15) McCleese et al., NatureGeo., v1, 2008.
- (16) Roble, Geophys. Monograph Ser, v87, 1995.
- (17) Parkinson and Hunten, JAS, 29, 1972.
- (18) McElroy and Donahue, Science, 177, 1972.
- (19) Shimazaki, Plan. Space Sci., v29, 1981.
- (20) Nair et al., Icarus, v111, 1994.
- (21) Montmessin&Lefèvre, NaturGeo, 2013.
- (22) Bates&Nicolet, JGR, v55, 1950.
- (23) Kaye, JGR, v93, 1988.
- (24) García-Muñoz et al., Icarus, v176, 2005.
- (25) Piccioni et al., JGR, v114, 2009.
- (26) Krasnopolsky, Icarus, v207, 2010.
- (27) Clancy et al., BAAS, v45, 2013.